Available online at www.sciencedirect.com
SCIENCE DIRECT
Journal of Catalysis 239 (2006) 410–421
JOURNAL OF CATALYSIS
www.elsevier.com/locate/jcat

Role of P-containing species in phosphated CeO_2 in the deterioration of its oxygen storage and release properties

M. López Granados [a,*], F. Cabello Galisteo [a], P.S. Lambrou [b], R. Mariscal [a], J. Sanz [c], I. Sobrados [c], J.L.G. Fierro [a], A.M. Efstathiou [b,*]

[a] *Instituto de Catálisis y Petroleoquímica, CSIC, C/ Marie Curie 2, Cantoblanco, 28049 Madrid, Spain*
[b] *Department of Chemistry, Heterogeneous Catalysis Laboratory, University of Cyprus, P.O. Box 20537, CY 1678, Nicosia, Cyprus*
[c] *Instituto de Ciencias de Materiales de Madrid, CSIC, Cantoblanco, 28049 Madrid, Spain*

Received 14 December 2005; revised 10 February 2006; accepted 12 February 2006

Available online 23 March 2006

Abstract

The chemical nature of P-containing species incorporated on the surface and within the subsurface regions of CeO_2 solid and their effects on the deterioration of the oxygen storage and release properties of phosphated ceria have been investigated. The samples were characterised by X-ray diffraction, X-ray photoelectron, Raman, and ^{31}P nuclear magnetic resonance spectroscopies; Fourier transform infrared pyridine chemisorption, N_2 physical adsorption isotherms, oxygen storage capacity, and $^{18}O_2$ temperature-programmed isotopic exchange measurements. In the samples with P/Ce ratios <0.03, isolated orthophosphate species are present on the surface and in the subsurface regions of CeO_2 solid. In these samples, deterioration of the oxygen storage and release properties correlates very well with the amount of P incorporated as isolated orthophosphates, because oxygen diffusion within the subsurface region of CeO_2 is increasingly inhibited. These results show that the presence of $CePO_4$ (monazite) is not essential for the deterioration of oxygen storage and release properties in CeO_2. In the samples with P/Ce > 0.03, crystals of monazite are formed. Theoretical estimations indicate that about 5.5 P atoms/nm^2 are required to fully cover the CeO_2 surface. This is equivalent to a P/Ce ratio of 0.02 in the ceria solid studied in the present work (BET area = 12.8 m^2/g). The experimental P/Ce ratio needed for complete surface saturation is higher (close to 0.03) very likely because part of P is incorporated into the subsurface region of ceria. Monazite also deteriorates the oxygen storage and release properties of ceria because it is a very stable Ce(III) phase. Once $CePO_4$ crystals are formed, further incorporation of P does not result in a deeper deterioration of the oxygen storage and release properties of ceria. Larger monazite crystals are then formed on the surface at the expense of isolated orthophosphate species, leaving part of the ceria surface uncovered and thus available for surface and bulk oxygen exchange.

Keywords: TWC deactivation; $CePO_4$; Monazite; Ceria oxygen storage and release properties; NMR; XPS; XRD; Pyridine adsorption; Fourier transform infrared; Oxygen isotopic exchange

1. Introduction

The presence of $CePO_4$ (monazite), a Ce(III) phase, has been noted as a severe cause of deactivation of vehicle-aged three-way catalysts (TWCs) [1–5]. The phosphorous involved in the formation of monazite arises from the decomposition of zinc dialkyldithiophosphate (ZDDP) present in the engine combustion chamber. ZDDP is an antiwear and antioxidant additive of lubricant oils. The phosphorous is transported to the monolith through the exhaust gases as P_2O_5 or H_3PO_4 [5–8], reacting with CeO_2 and $Ce_xZr_{1-x}O_2$ solid solutions present in the wash-coat, leading eventually to the formation of $CePO_4$.

CeO_2 and, more recently, its derived $Ce_{1-x}Zr_xO_2$ solid solutions are considered essential components for the correct functioning of TWC under the rapid oscillations of the exhaust gas composition around the stoichiometric A/F value [9–11]. In particular, these oxides show remarkable oxygen storage and release (OSR) properties; that is, they can buffer the oscillation of the O_2 concentration during the rich or lean excursions of the

* Corresponding authors. Fax: +34 91 5854760 (M. López Granados), +35722 892801 (A.M. Efstathiou).
E-mail addresses: mlgranados@icp.csic.es (M. López Granados), efstath@ucy.ac.cy (A.M. Efstathiou).

0021-9517/$ – see front matter
doi:10.1016/j.jcat.2006.02.007

exhaust gas because of their ability to rapidly release or capture oxygen species. This property has been quantified by measurement of the amount of oxygen that can be taken from the oxide by the reducing agent (CO or H_2) or captured by the solid after reducing treatments [12], and is termed oxygen storage capacity (OSC). OSC is quantified using pulses or fast-step gas concentration switches between oxidizing and reducing gas mixtures. It has been claimed that formation of monazite has a negative impact on the OSR properties of Ce oxides [5,13], because the monazite is a very stable Ce(III) phosphate compound that cannot participate in rapid redox Ce(IV)/Ce(III) processes required for the OSR and the fast response during rapid oscillations of the exhaust gas composition.

In general, the negative effect of $CePO_4$ on the OSR properties of Ce oxides has been established. However, additional research is still needed to understand in depth the chemical and structural reasons behind this phenomenon. Various questions still remain to be answered, particularly the mechanism by which the OSR properties are affected by P-containing species (e.g., surface oxygen activation, surface oxygen diffusion, oxygen anion bulk diffusion, oxygen vacancy diffusion) and the exact location (surface or bulk) of P-containing species.

In previous work we have demonstrated that large $CePO_4$ crystals are formed by P incorporation to Ce oxides [13,14]. The monazite crystals occupy surface and subsurface regions of Ce oxides, but parts of them are uncovered and thus accessible to OSR processes. In principle, this may lead to the conclusion that deterioration of such important properties of ceria is due to the lower number of surface sites available for oxygen activation and exchange. However, the incorporation of phosphorous within the ceria crystal structure can cause inhibition of anion conductivity [15] and, accordingly, of the proper functioning of the OSR properties.

In an attempt to gain more fundamental information on the surface and bulk chemical character of incorporated phosphorous in ceria, different amounts of P have been used. The phosphated ceria samples thus prepared have been characterized using various techniques to identify the chemical nature of P species and the surface and/or bulk location. In addition, the deterioration of the OSR properties of ceria has been correlated with the amount and location of P-containing species in the CeO_2 solid.

2. Experimental

2.1. Preparation of phosphated-CeO_2 materials

CeO_2 was prepared by precipitation from an aqueous solution containing $Ce(NO_3)_3$ after adding a dropwise aqueous solution of NH_4OH (3 N) under vigorous stirring up to a pH value of 10. After precipitation, the obtained hydroxide was filtered, extensively washed with deionised water, and then dried at 383 K for 24 h. The solid thus obtained was calcined in air at 873 K (heating rate 5 K/min) for 12 h, cooled to room temperature, and then divided into several portions before storage. A fraction of the sample was recalcined for another 12 h at 873 K (5 K/min). The solid thus obtained was labelled Ce. Another portion of the sample was impregnated with phosphorus according to the following procedure. A given amount of $(NH_4)_2HPO_4$ was dissolved in water, and the obtained solution was poured into a flask containing the Ce oxide, so as to yield atomic ratios of P/Ce = 0.01, 0.02, 0.05, 0.1, and 0.2. The suspension was then smoothly stirred for 2 h, and the excess water was evaporated in a rotary evaporator at 333 K ($P < 0.1$ atm). The P-containing samples were then calcined in air at 873 K (5 K/min) for 12 h and labelled CeP0.01, CeP0.02, CeP0.05, CeP0.1, and CeP0.2. It is important to note here that the amount of P remaining in each of the solids after calcination in air was less than the nominal amount used during the preparation procedure. For the sake of simplicity, nominal values were kept in the labelling of the samples.

2.2. Characterisation of solids

2.2.1. Total reflection X-ray fluorescence analyses

Total reflection X-ray fluorescence (TXRF) analyses were performed on a Seifert EXTRA-II spectrometer (Rich Seifert, Ahrensburg, Germany) equipped with two X-ray fine-focus lines, Mo and W anodes, and a Si(Li) detector of an active area of 80 mm^2 and resolution of 157 eV at 5.9 keV (Mn-K_α). A tungsten X-ray source was used for P determination. Radiation was filtered with a 10-μm-thick Cu film to optimise the energy range (0–10 keV) used in the analyses. A molybdenum X-ray source was used for the analysis of Ce, previously filtered with a Mo film of 50 μm. A 10-mg sample was ground to powder form in an agate mortar, resulting in a particle size <30 μm. The powder was then ground for another 20 min in a vibrating micropulveriser (having a ball and a base of agate) in the presence of 1 ml of high-purity water. Next, the mixture was poured into a test tube in which up to 2 ml of high-purity water was added. The sample was homogenized for 10 min by ultrasonic treatment to disperse possible agglomeration of particles. Then 2 μl of the suspension was placed on a flat plastic carrier where the water was evaporated under vacuum. Assuming that some of the P or Ce cations were leached during the homogenisation, these elements would have been again deposited back onto the solid surface after evaporation of water. Further details of the analysis conditions have been described elsewhere [1,16].

2.2.2. X-Ray photoelectron spectroscopy studies

X-Ray photoelectron spectroscopy (XPS) studies were performed with a VG Escalab 200 R spectrometer equipped with a hemispherical electron analyzer and a Mg-K_α (1253.6 eV) X-ray source. The sample was first placed in a copper holder mounted on a sample-rod in the pretreatment chamber of the spectrometer. It was then outgassed at room temperature for 1 h before being transferred to the analysis chamber. A given region of the XPS spectrum was scanned a number of times to obtain a good signal-to-noise ratio. The binding energies were referenced to the spurious C 1s peak (284.6 eV) used as an internal standard for charging effects. The areas of the peaks were computed by fitting the experimental spectra to Gaussian/Lorenztian curves after removing the background (us-

ing the Shirley function). Surface atom ratios were calculated from peak area ratios normalized by using the corresponding atomic sensitivity factors [17]. The error in the calculation of surface atom ratios is considered <5%.

2.2.3. X-Ray diffraction studies

Powder X-ray diffraction (XRD) patterns were recorded in the 5°–85°2θ range in the scan mode (0.02°, 1 s) using a Seifert 3000 XRD diffractometer equipped with a PW goniometer with Bragg–Brentano $\theta/2\theta$ geometry, an automatic slit, and a bent graphite monochromator.

2.2.4. Raman spectroscopy studies

Raman spectra were recorded with a Renishaw 1000 spectrophotometer equipped with a cooled (200 K) CCD detector and a holographic notch filter to remove the elastic scattering. Samples were excited with the 514-nm Ar line. Spectra acquisition consisted of 5 scans of 60-s duration for each sample. All samples were pretreated in dry air at 676 K (100 NmL/min, 60 min) in an in situ cell (Linkam, TS-1500) before the spectra were recorded at 473 K under dry air flow.

2.2.5. Nuclear magnetic resonance studies

^{31}P MAS nuclear magnetic resonance (NMR) spectra were recorded at room temperature in an Avance-400 Bruker spectrometer (9.4 Tesla). The frequency used for ^{31}P was 161.97 MHz. Samples were spun at 8 kHz during signal recording. Spectra were obtained after $\pi/2$ pulse irradiation (∼4 μs) with a recycling time of 5 s. The number of scans was in the range of 40–800. ^{31}P chemical shift values were estimated relative to 85 vol% H_3PO_4 aqueous solution. Errors in band positions were <0.5 ppm.

The NMR spectra were fitted with the Bruker WINFIT software package [18]. This program allowed determination of the position, line width, and intensity of the spectra components with a nonlinear least squares iterative method. For quantitative purposes, the sum of integrated intensities of the spinning side bands associated with each component was determined. Errors in the determination of relative band intensities are considered <2%.

2.2.6. BET surface area measurements

Nitrogen adsorption isotherms were recorded at 77 K using a Micromeritics ASAP 2000 apparatus. Before determination of an adsorption isotherm, the sample was degassed at 413 K for 12 h.

2.2.7. Fourier transform infrared spectroscopy of adsorbed pyridine

Pyridine Fourier transform infrared spectra were recorded with a Nicolet 5ZDX Fourier transform infrared spectrophotometer at a resolution of 4 cm^{-1} over the entire spectral range and averaged over 128 scans. The samples were pressed into self-supporting wafers (ca. 10 mg/cm^2), placed in a sample holder, and pretreated in an infrared cell designed to work under vacuum or dynamic conditions. The samples were calcined in room air at 873 K for 1 h and then outgassed at 873 K for 1 h. After cooling to 393 K, the samples were outgassed (5×10^{-5} Torr) for 30 min. The samples were then exposed to 5 Torr of pyridine for 5 min at room temperature and evacuated for 30 min at this temperature (to remove physisorbed pyridine), after which the spectra were recorded. The presented infrared spectra were obtained after subtracting the solid sample background spectrum obtained under vacuum from the initially recorded spectrum after pyridine chemisorption.

2.2.8. Transient oxygen storage and release studies

The capability of the investigated solids to store and release both surface and bulk oxygen species was measured by two different transient techniques. The first technique gives the amount of oxygen that can be stored by the solid after reductive treatment at a given temperature by CO or H_2 pulses; the second technique, termed temperature-programmed isotopic exchange (TPIE), probes the exchange capability of surface or bulk lattice oxygen of the solid with gas-phase oxygen.

2.2.8.1. OSC measurements The OSC (μmol-O/g_{cat}) of CeO_2 samples containing phosphorus (P/Ce = 0.0–0.2) was measured after using the pulse injection method [19]. The transient flow system, the microreactor, and the mass spectrometer used have been described elsewhere [20]. The reactive oxygen species present in the solid is estimated through the amount of H_2 consumed during the reduction or the amount of O_2 consumed during the reoxidation stage [19,21]. The latter amount of oxygen is referred to the oxygen storage capacity complete (OSCC). The amount of the most reactive oxygen (labile oxygen) of the catalyst is defined as the amount of oxygen species that reacts during the first H_2 pulse, known as the OSC.

The amount of catalyst sample used for the pulse injection experiments was 100 mg in powder form. The general experimental procedure applied for measuring the oxygen storage capacity by pulse injection experiments was as follows. The catalyst sample was initially pretreated with a 20% O_2/He gas mixture at a given temperature (T_{OSC}) for 1 h (heating rate of 10 K/min from room temperature to T_{OSC}). The reactor was then flushed with He for 15 min at T_{OSC}, followed by H_2 pulse(s). For OSC measurements, the catalyst sample was reacted with only one H_2 pulse (50 μmol) and then reoxidized with several successive pulses of O_2 (one oxygen pulse equals 10 μmol of O_2) at the same temperature. For OSCC measurements, the sample was reacted with several successive pulses of H_2 (until no consumption was observed) and then reoxidized with several successive pulses of O_2.

2.2.8.2. $^{18}O_2$ isotopic exchange studies TPIE experiments were conducted as follows. After calcination of the fresh sample (100 mg) at 873 K in air for 2 h, the reactor was flushed in He at 873 K for 15 min to remove oxygen from the gas phase and the gas lines. The reactor was then cooled in He flow to 300 K, and the feed was switched to a 3 mol% $^{16}O_2$/He gas mixture for 15 min. A switch to the equivalent isotopic 3 mol% $^{18}O_2$/He gas mixture (Isotec, 97 at% ^{18}O) was then made, while at the same time the temperature of the solid was increased to 1073 K at a rate of 30 K/min. All three oxygen isotopic species

[$^{18}O_2$ ($m/z = 36$), $^{16}O^{18}O$ ($m/z = 34$), and $^{16}O_2$ ($m/z = 32$)] were monitored continuously with an on-line quadrupole mass spectrometer (Omnistar 300, Balzers) equipped with a fast-response inlet capillary/leak valve (SVI 050, Balzers) system [20].

3. Results

3.1. Chemical characterisation of solids

Fig. 1 presents the P/Ce ratio in the solids determined by the TXRF technique as a function of the P/Ce ratio used in sample preparation. P/Ce ratios are always found to be below the nominal values; the continuous line (theoretical) is above the experimental curve. This indicates that part of P is lost during the calcination procedure (up to 873 K). It is noted that phosphorous oxides have boiling points close to the calcination temperature. Moreover, a change in the slope has been observed around the nominal value of P/Ce = 0.05 (experimental P/Ce ∼ 0.03). The P/Ce ratios of CeP0.01 and CeP0.02 samples, although below the solid line, are found to be closer to the nominal values. In contrast, the P/Ce ratio values of the rest of the samples are well apart from the solid line (Fig. 1).

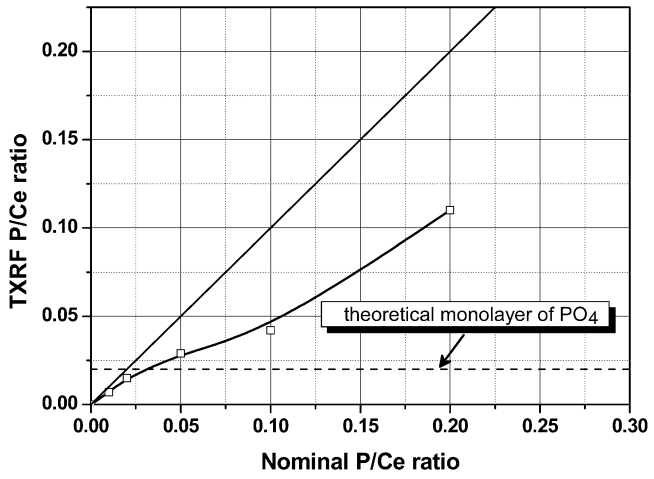

Fig. 1. Experimental P/Ce ratios obtained by TXRF analyses as a function of the nominal P/Ce ratios used in the preparation procedure of the phosphated ceria samples.

Fig. 2a presents XPS spectra of the Ce $3d_{5/2}$ and Ce $3d_{3/2}$ core levels for all solids investigated. The Ce 3d signal of Ce sample corresponds to that of Ce(IV) in CeO_2 [22–26]. According to the assignment proposed by Burroughs et al. [27], the $3d_{3/2}$ multiplets signals of Ce(IV) are labelled U, U″, and U‴, whereas those of $3d_{5/2}$ are labelled V, V″, and V‴. The Ce(III) signal exhibits four peaks (U_0, U′, V_0, and V′). In the CeP0.2 sample, the XP core level is dominated by the Ce(III) features; however, some Ce(IV) still exists at the surface of CeO_2, as indicated by the weak peak at ca. 917 eV [22–26]. These results indicate that the surface of CeP0.2 solid is greatly covered by $CePO_4$ [3,13]. For samples with lower P/Ce ratios, the XP spectra progressively change and Ce(IV) features are more visible.

A semiquantitative estimation of Ce(IV) concentration at the surface of the solids can be performed based on the ratio between the integrated area of the well-resolved peak U‴ and the total area of the Ce 3d level [22–24,28–30]. This peak is very weak in CeP0.2 sample (representing 5.9% of the area of all of the peaks) and grows progressively with decreasing

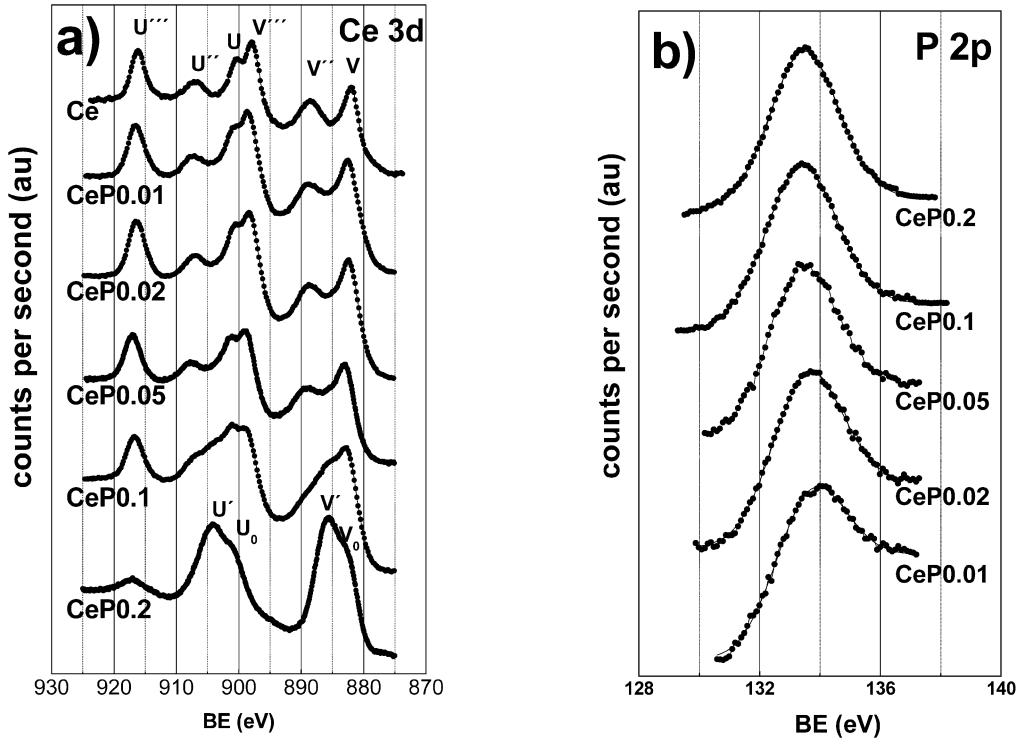

Fig. 2. X-Ray photoelectron spectra of Ce 3d (a) and P 2p (b) core levels corresponding to the different solid samples. U, U″, U‴, V, V″, and V‴ labels indicate the position of the Ce(IV) 3d multiplets, whereas U_0, U′, V_0, and V′ indicate those of Ce(III).

P/Ce ratio. This indicates that Ce(IV) species become increasingly concentrated at the surface of the samples as the amount of incorporated P in the sample decreases. In the CeP0.01 and CeP0.02 samples, the intensity of the U‴ peak (around 13.5% of the total area) is very close to that of the Ce sample. This suggests that the amount of Ce(IV) present at the surface of the CeP0.2 sample is almost half than that found in the CeP0.01 or CeP0.02 samples.

The XPS spectra of the 2p core level of samples are presented in Fig. 2b. The binding energy is consistent with the presence of PO_4 units. The XPS peaks of the samples with P/Ce < 0.03 are asymmetric. In the CeP0.01 sample, the presence of a second peak is more evident at the high-binding energy side. This suggests the presence of two different P species in the samples of low P/Ce ratios.

Fig. 3 presents the P/Ce surface atomic ratio determined by XPS versus the experimental P/Ce ratio determined by TXRF analyses. The dotted line represents hypothetical solids in which the surface P/Ce ratio determined by XPS is equal to the bulk ratio (TXRF value), and represents those solids in which P is not restricted to the surface, but rather is homogeneously incorporated within the solid. The fact that all P/Ce ratios of the samples are above the dotted line is a result of the preferential location of P in the outermost region of the solid. The question that remains is whether P is restricted to the outermost layer or can also be located deeper in the subsurface region of the solid. NMR results will give support to this hypothesis.

Fig. 4 shows XRD patterns of the different samples investigated. In all of the samples, reflections due to the cubic CeO_2 structure are clearly visible (marked as "1" in Fig. 4). In the CeP0.1 sample and especially the CeP0.2 sample, the peaks of the monazite (JCPDS file 83-0650) can also be observed (marked as "2" in Fig. 4). In the samples with lower P/Ce ratios, $CePO_4$ peaks were not detected.

Fig. 5 displays the Raman spectra of the solid samples. The three bands visible in the spectra of Ce sample (a strong band at 464 cm^{-1} and weaker bands at 242 and 1180 cm^{-1}) correspond to those of cubic CeO_2 phase [13]. The CeP0.2, CeP0.1, and CeP0.05 samples show additional weak bands at 969, 990, 1051, and 1066 cm^{-1} associated with the $CePO_4$ phase [5,13, 31–33]. It must be stressed that these bands start to become visible in the CeP0.05 solid sample, whereas monazite is not detected by XRD. This indicates that the crystal size of Ce phosphate is beyond the detection limit of the XRD used and/or that the crystallization of this solid phase is poor. From this fact, we can conclude that CeP0.05 solid can be considered a border-

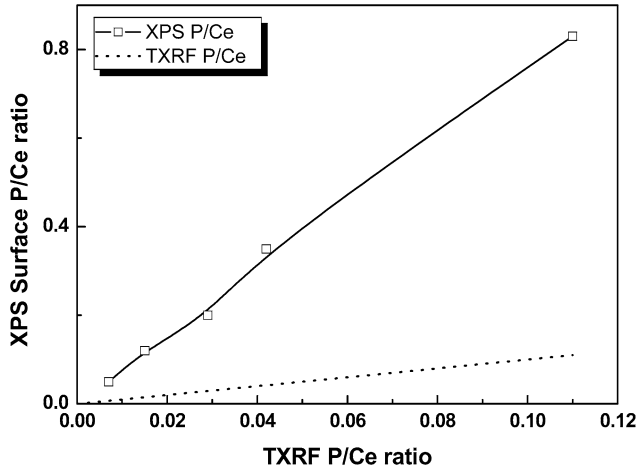

Fig. 3. Surface P/Ce ratio (□) determined by XPS as a function of the experimental P/Ce ratios determined by TXRF. Dotted line represents solid materials the surface P/Ce ratio of which is equal to the bulk P/Ce ratio.

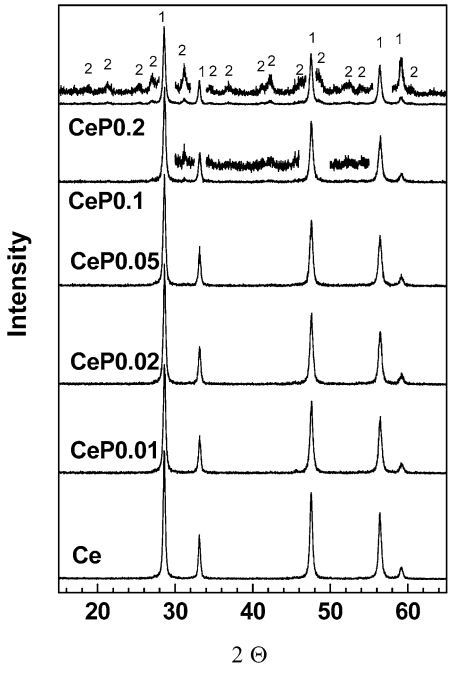

Fig. 4. X-Ray diffraction patterns of the investigated Ce, CeP0.01, CeP0.02, CeP0.05, CeP0.1, and CeP0.2 solids.

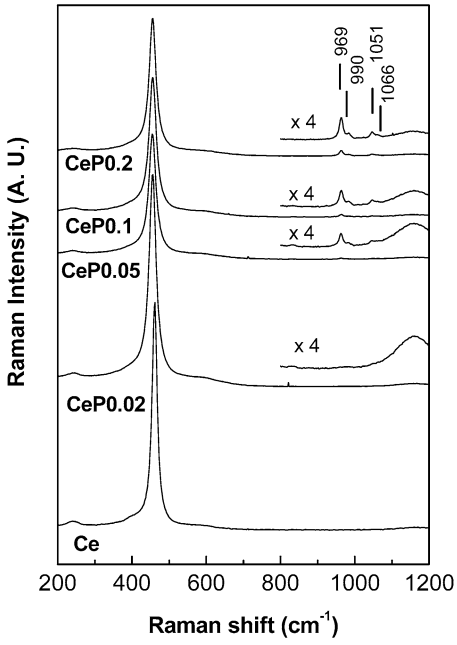

Fig. 5. Raman spectra in the 200–1200 cm^{-1} range of the investigated Ce, CeP0.02, CeP0.05, CeP0.1, and CeP0.2 solids.

line sample with low P incorporation, where $CePO_4$ features cannot be detected by XRD.

Fig. 6 shows ^{31}P MAS NMR spectra of five samples recorded at room temperature. In the samples with lower P content (CeP0.01 and CeP0.02), spectra are formed by several narrow lines centered near 0 ppm. In the samples with high P content (CeP0.1 and CeP0.2), spectra are formed by a broad component modulated by equal-spaced spinning side bands associated with the rotation of the sample. The central component of this signal is centered at −100 ppm. In the CeP0.05 sample, the NMR spectrum is formed by these two components. A small contribution of the signal centered near 0 ppm can also be seen in the CeP0.1 sample, overlapped to the main signal centered at −100 ppm. Fig. 7 shows a magnification of the central band of the CeP0.01, CeP0.02, and CeP0.05 samples. The spectra shown are formed by four components at 0.71, −3.2, −5.9, and −8.6 ppm. The intensity of the last three bands increases at the expense of the intensity of first component when the amount of P incorporated in the sample increases. In the CeP0.05 sample, the line width of components increased considerably, and resolution of the four components was not possible.

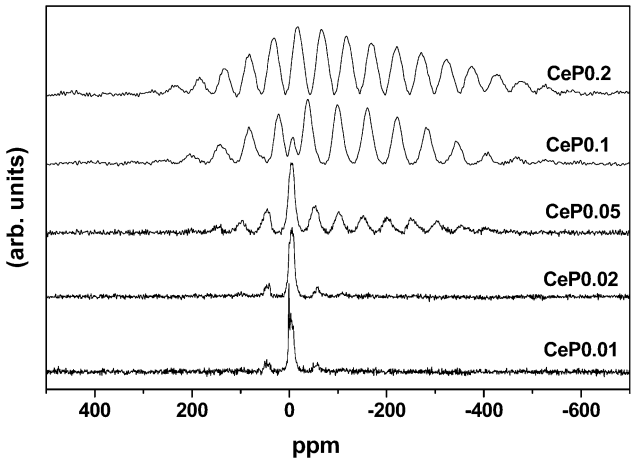

Fig. 6. ^{31}P magic angle spinning nuclear magnetic resonance spectra of the CeP0.01, CeP0.02, CeP0.05, CeP0.1, and CeP0.2 investigated solids.

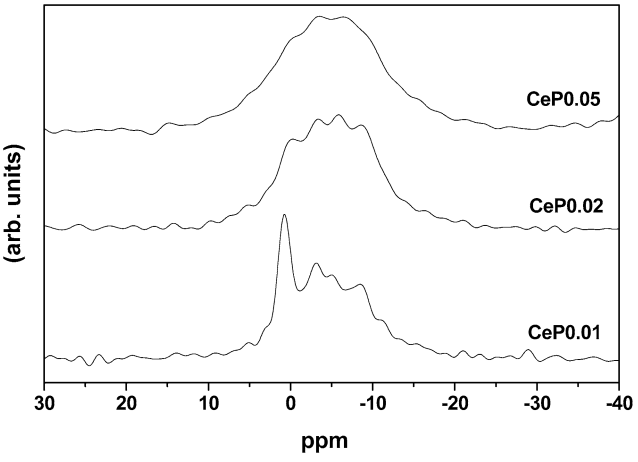

Fig. 7. Magnification of the central bands presented in Fig. 6 for the CeP0.01, CeP0.02, and CeP0.05 solids.

Comparing ^{31}P MAS-NMR spectra of the five samples investigated shows that species formed on the CeO_2 surface are different with respect to the low- and high-P content samples. In the first case, chemical shift values of components near 0 ppm correspond to orthophosphate species (PO_4 units) [34–36]. These signals are ascribed to isolated orthophosphate species interacting with the surface of CeO_2. The intensity of the new components at −3.2, −5.9, and −8.6 ppm increases at the expense of that at 0.71 ppm when the amount of incorporated P in ceria solid increases. Taking into account that the chemical shift values become more negative with increasing amounts of Ce(IV) cations sharing oxygen atoms with the PO_4 tetrahedron, the three signals with negative shifts can be ascribed to orthophosphate species with greater numbers of P–O–Ce bonds. This gives support to the hypothesis that P has penetrated into the bulk of the solid, because an increased number of P–O–Ce bonds is possible only if P is located deeper in the bulk.

Based on the foregoing observations and discussion, it can be concluded that the engagement of P tetrahedra with CeO_2 increases with increasing P content, as does the P concentration in the subsurface region. With this in mind, the hypothesis of the existence of two types of isolated PO_4 species in the samples of low P/Ce ratios, one on the surface with a small number of P–O–Ce bonds and another in the subsurface region with larger number of P–O–Ce bonds, may be related to the detection of two different P 2p core-level XP peaks in these samples. The first of these peaks, at the high binding energy, could be assigned to the surface species, and the second, at the lower binding energy, could be assigned to the inner species. The latter becomes predominant as P loading increases.

In samples with high P content, the broad component undergoes an up-field shift to −100 ppm. It is known that the presence of paramagnetic centers shift NMR signals toward more negative values. Accordingly, the broad component can be ascribed to $CePO_4$ in which all cerium atoms are trivalent and display a paramagnetic moment. This assignment is supported by the XRD and Raman results obtained in this work. This means that nucleation of $CePO_4$ is favored when the amount of phosphoric acid used in the preparation increases. It must be stressed that the formation of $CePO_4$ brings about reduction of Ce(IV) to Ce(III), which is consistent with the well-known stability of $CePO_4$ at high temperatures with respect to other Ce(IV) phosphates [37,38]. This is consistent with the important up-field shift detected in CeP0.1 and CeP0.2 samples. It is also interesting to note that in the CeP0.1 sample, a small percentage of deposited species remains as isolated orthophosphates, whereas most of these species are incorporated as $CePO_4$.

3.2. $CePO_4$ nucleation

The aforementioned considerations suggest that $CePO_4$ nucleation occurs by agglomeration of orthophosphate species in certain domains of CeO_2 surface. An estimation of the amount of PO_4 tetrahedra that can be geometrically deposited on any support surface has been performed after assuming that the area occupied by any tetrahedron is the kinetic area of a face of

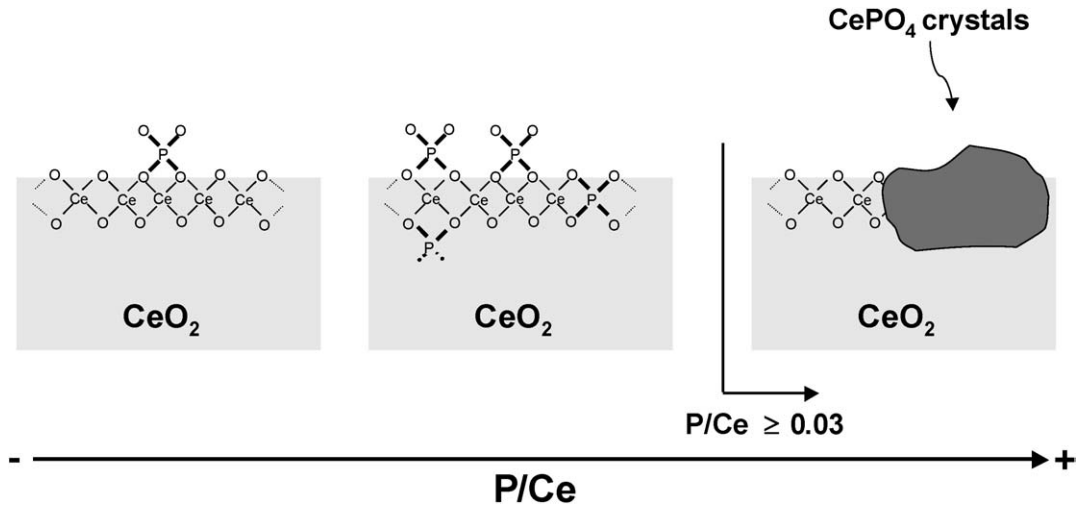

Scheme 1. Schematic representation illustrating the progressive formation of $CePO_4$ from individual PO_4 tetrahedra (Ce ions are eight fold coordinated).

tetrahedron, which is $2^{1/3}$ times the geometric area [39]. The average O–O distance in the $CePO_4$ has been used in this calculation [40]. The kinetic area of a tetrahedron was estimated to be 0.18 nm^2, which implies that 5.5 PO_4 units per nm^2 are required to geometrically cover the support surface. This value is close to that needed to cover the surface of γ-alumina by PO_4, which was reported to be 5.1 PO_4/nm^2 [41].

Taking into account the specific surface area of CeO_2 (12.8 m^2/g), the P/Ce ratio needed to cover this surface, assuming that P is restricted to the surface, can be estimated as 0.02 (formation of a monolayer). The broken line in Fig. 1 represents this case; below this theoretical value, the solid samples have an insufficient experimental P content to cover the surface of CeO_2 by PO_4 units. In contrast, samples with P content above this value have sufficient P to theoretically cover the surface. It is worth mentioning that this value is close to the experimental P/Ce ratio (P/Ce = 0.03) detected by TXRF in the CeP0.05 sample. This sample represents a change in the trace of the curve in Fig. 1 and is the sample in which $CePO_4$ starts to be detectable by Raman and ^{31}P NMR techniques.

Consequently, according to the present data, the following model of interaction between P-containing species and CeO_2 can be proposed. When a low level of P is incorporated in CeO_2, isolated PO_4 units are deposited on the surface, increasing the engagement with Ce(IV) as P/Ce increases. Phosphorous is not restricted only to the outermost surface layer, but is also present in the subsurface region. In principle, one should expect that anchored orthophosphate units exhibit a low coordination number with Ce(IV) cations, whereas those located deeper in subsurface regions should exhibit higher coordination numbers with Ce(IV) cations, in agreement with the ^{31}P NMR data obtained.

When P/Ce increases, the surface region becomes saturated by orthophosphate species, and crystals of $CePO_4$ start to nucleate. This situation is firstly reached in the case of CeP0.05 sample that presents an experimental value of P/Ce ratio of 0.03. In principle, one might expect $CePO_4$ crystals to be detectable in samples with lower experimental P/Ce ratios (e.g., P/Ce = 0.02); however, the partial penetration of P inside the solid may explain this observation. Beyond this point, the concentration of orthophosphate species is so high that their existence is not possible, and $CePO_4$ now becomes the stable phase. Larger $CePO_4$ crystals are formed when larger amounts of P are incorporated. This model of interaction between P-containing species and ceria solid can be summarised in the simplified Scheme 1. A more accurate structural description of the arrangement of orthophosphate units within the bulk of ceria cannot be made with the characterisation results obtained and presented herein and is beyond the scope of this work.

It is important to note at this point that the Ce–O–P phase diagram is far from well understood. The preparation method [42], the nature of precursor compounds used for P and Ce [43], the temperature at which synthesis occurs, and the atomic P/Ce ratio used [37,38,44,45] appear to be important variables for obtaining the final form of Ce phosphate. Most of the studies in the literature [37,38,44,45] have focused on the preparation of Ce phosphates with P/Ce ratios >1. In such cases, along with monazite, other phases, including CeP_2O_7 and $Ce(PO_3)_3$, have been obtained at synthesis temperatures similar to those used in the present work. These results illustrate that the Ce–P–O system is not so simple and that monazite does not necessarily dominate in the phase diagram. To the best of our knowledge, preparation of Ce phosphates with P/Ce ratios smaller than unity has not yet been reported.

3.3. Surface characterization of solids

Infrared spectroscopy was used to obtain a more detailed picture of the surface structure of P-doped ceria samples. Adsorbed probe molecules, such as pyridine, have been widely used to investigate the properties of the ceria surface, namely coordinatively unsaturated Ce(IV) (Lewis acid sites), and O^{2-} (basic sites). According to previous reports [46–48], pyridine coordinated to Lewis acid sites gives specific bands in the 1634–1595 cm^{-1} range (mode ν8a). This mode is very sensitive to the strength of the Lewis acid sites. In contrast, the intensity of the band at 1464–1440 cm^{-1} (mode ν19b) is suitable for estimating the number of these sites. Pyridine molecules chemisorbed on Brönsted acid sites also display infrared bands

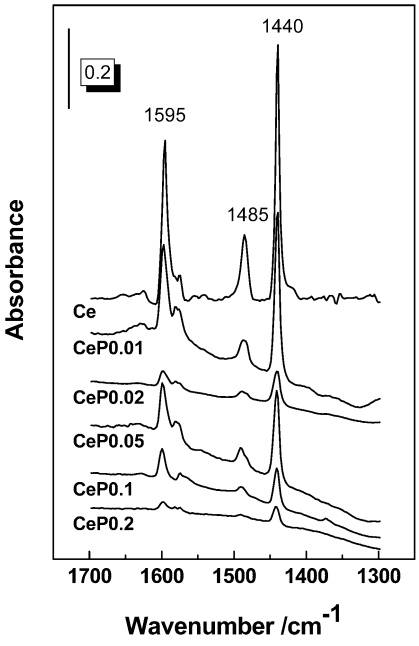

Fig. 8. FT-IR spectra of pyridine chemisorbed on the investigated Ce, CeP0.01, CeP0.02, CeP0.05, CeP0.1, and CeP0.2 solids.

at 1530–1550 and 1610–1640 cm^{-1}, with the former being the most intense [46–48]. At this point, it is appropriate to stress that pyridine adsorption on Lewis acid sites can be used to estimate the relative amount of Ce(IV) coordinatively unsaturated surface sites (CUS) of Ce oxide. This characterization is relevant not only for quantitative purposes, but also for improving understanding of the OSR properties, because O exchange between the gas phase and Ce oxide requires the presence of these CUS sites to activate the gaseous oxygen molecules [49].

Fig. 8 shows infrared spectra of pyridine chemisorbed on Ce and CeP samples. After adsorption of pyridine, only bands due to molecularly adsorbed pyridine were observed [50]; no infrared bands of pyridine chemisorbed on Brönsted acid sites were visible. For P-containing samples, the frequency of the 8a mode (1595 cm^{-1}) was not shifted with increasing phosphorous concentration, indicating that Ce(IV) ions presented similar acidic strengths on the surfaces of pure ceria and of P-containing samples. The amount of exposed Ce(IV) sites was estimated by plotting the intensity of the mode ν19a (1440 cm^{-1}) versus P content (Fig. 9). At low phosphorous content (P/Ce < 0.02), the intensity decreases with increasing P content, suggesting a decreasing number of unsaturated exposed Ce(IV) surface sites due to P incorporation into ceria solid. The CeP0.05 sample (experimental P/Ce ratio $= 0.03$) represents a discontinuity in the observed trend, indicating that the surface of this sample is different than that of the samples with lower P content, in which the number of exposed Ce(IV) surface sites was higher. For samples with higher P content, the area of the infrared band was decreased (Fig. 9).

The same tendency was observed for the specific surface area of the solids (Fig. 10). Adding small amounts of P resulted in a slight increase in specific surface area (CeP0.01 sample) with respect to bare CeO_2. On the other hand, further addition of P resulted in decreased BET area. This tendency was not seen

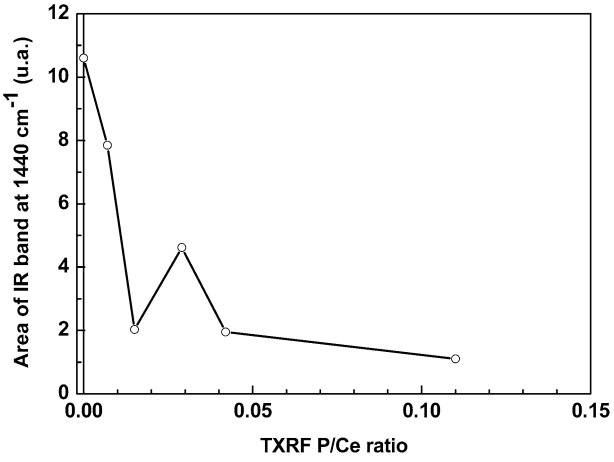

Fig. 9. Correlation of the area of the infrared band at 1440 cm^{-1} as a function of the experimental P/Ce ratio determined by TXRF.

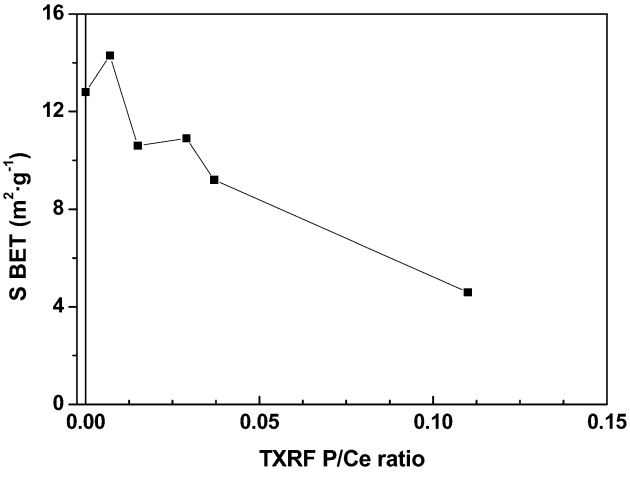

Fig. 10. Variation of the specific surface area (BET) of the different solids as a function of the experimental P/Ce ratio determined by TXRF.

in the CeP0.05 sample, which has a BET surface area similar to that of the CeP0.02 sample. Beyond this value, a downward trend was seen, and the specific surface area decreased with increasing P concentration. This break in the monotonous trend observed in Figs. 9 and 10 for the CeP0.05 sample is in agreement with the nucleation of $CePO_4$ that starts to be visible in this sample and results in a rearrangement of its surface.

3.4. OSR properties of P-containing ceria solids

3.4.1. OSC measurements

Fig. 11 presents results of OSC measurements (μmol-O/g_{cat}) conducted at T_{OSC} in the 673–873 K range using H_2 and O_2 pulses over different samples. In an attempt to estimate the surface or bulk origin of the oxygen species titrated in this experiment, the amounts of equivalent numbers of oxygen monolayers corresponding to the OSC values were calculated. This quantity was estimated based on the theoretical density number of surface oxygen atoms for ceria (cubic, 13.1 atoms/nm^2) [51]. In all cases presented in Fig. 11, the number of equivalent oxygen monolayers is below or close to 1. This is an underes-

timation, because P is also present on the surface and within the subsurface region of the solid. Nonetheless, it can be concluded that oxygen species titrated by the OSC measurements arise mainly from the surface or from the near-subsurface region of the solid.

As indicated in Fig. 11, OSC increases with increasing temperature at which oxygen is stored (T_{OSC}). The same conclusion can be drawn for the OSCC values measured (results not presented here). This behaviour is expected, considering the fact that the kinetic rate constant (k) of the reaction of H_2 with stored oxygen species increases with temperature. In addition, by increasing the temperature (T_{OSC}), the amount of oxygen stored in CeO_2 solid through bulk diffusion is expected to increase, and thus the amount of H_2 consumed will also increase. Two facts are worth stressing here. First, there is an observable and continuous decrease in OSC measured over the P-contaminated solids compared with pure ceria. Second, once $CePO_4$ predominates over the surface, the rate of OSC depletion with increasing P/Ce ratio becomes small. Thus, although the amount of P incorporated in the CeP0.2 sample is much higher than that in the CeP0.1 solid, the two samples have similar OSC capacities.

3.4.2. $^{18}O_2$ isotopic exchange studies

Fig. 12 presents transient response curves of $^{16}O_2$(g) (a) and $^{18}O^{16}O$(g) (b) isotopic species obtained during the TPIE experiments. The highest temperature reached in the experiment was 1073 K, after which the experiment was conducted isothermally. The $^{16}O_2$ signal arises from the multiple heteroexchange mechanism of $^{18}O_2$(g) with the metal oxide solid surface as opposed to the simple heteroexchange mechanism [13,14]. As Fig. 12 clearly shows, the maximum rate of ^{18}O exchange with the surface ^{16}O species and the total amount of exchangeable oxygen of the P-containing solids were significantly reduced with an increasing P/Ce ratio, indicating a significantly depleted amount of exchangeable O due to P incorporation into the ceria solid. There was also a clear shift to higher temperatures in the appearance of the peak maximum obtained for the $^{16}O_2$ TPIE response curve with increasing P/Ce ratio. A shift to higher temperatures has been also described for other P-contaminated Ce and CeZr solids [14]. This shift may reflect either the increase in the activation energy of the bulk oxygen diffusion process or the decrease in the number of active sites involved in the exchange process; a similar feature can be seen in a temperature-programmed desorption profile with decreasing initial surface coverage. The exchange of O atoms from the surface/bulk of $CePO_4$ (monazite) crystals present in phosphated ceria solids must be excluded at the conditions of the TPIE experiments (Fig. 12) for several reasons. According to previous reports [52,53], the bulk diffusion coefficient of oxygen in monazite crystal at 923 and 1073 K is more than six orders of magnitude lower than that in CeO_2 crystals. Moreover, if the exchange rate of oxygen due to monazite or to orthophosphate species were significant, then a drastic decrease in the amount of exchangeable oxygen with increasing P/Ce ratio in ceria solid would likely not be expected. Therefore, the transient isotopic exchange results reported in Fig. 12 reflect the exchange of ^{18}O with ^{16}O only in CeO_2 and CeO_2-phosphated crystals, not in $CePO_4$ or orthophosphate species.

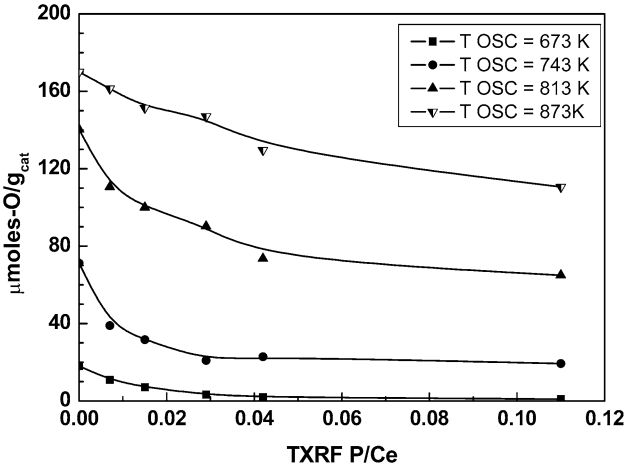

Fig. 11. OSC values (µmol-O/g_{cat}) measured over the Ce, CeP0.01, CeP0.02, CeP0.05, CeP0.1, and CeP0.2 solids by H_2 pulsed-feed experiments in the 673–873 K range as a function of the experimental P/Ce ratio determined by TXRF.

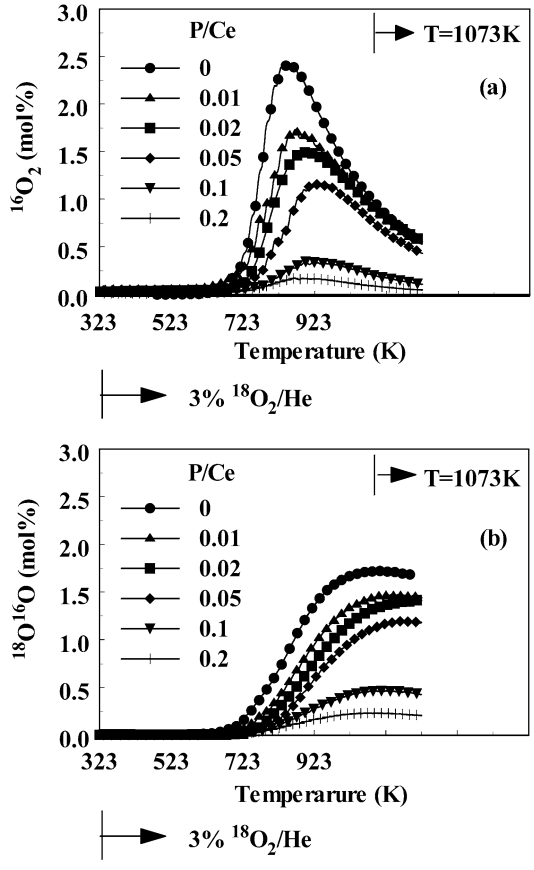

Fig. 12. Transient gaseous response curves of $^{16}O_2$ (a) and $^{18}O^{16}O$ (b) isotopic species obtained during TPIE experiments over the different solids (P/Ce = 0.0–0.2) according to the following gas delivery sequence: 20% O_2/He (873 K, 1 h) → He (873, 15 min) → cool down in He flow to 300 K→ 3% O_2/He (300 K, 15 min) → 3% $^{18}O_2$/He, T is increased to 1073 K (heating rate = 30 K/min).

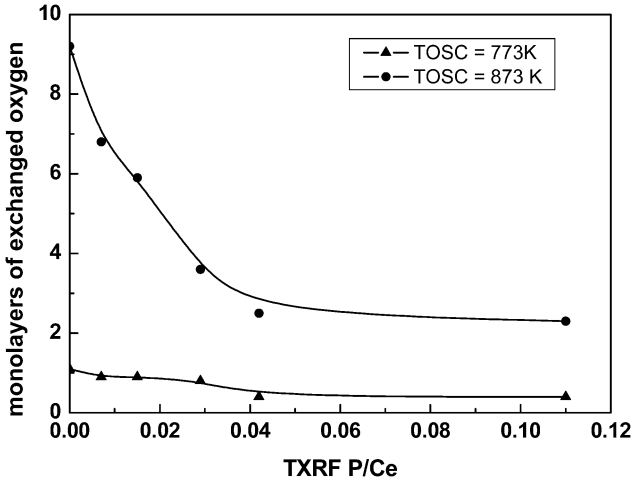

Fig. 13. Number of equivalent monolayers of atomic oxygen species exchanged during the TPIE experiment (Fig. 12) for the investigated solids.

Fig. 13 reports the number of equivalent monolayers of atomic oxygen species exchanged during the TPIE experiments (Fig. 12) for the six solids investigated. Only data from Fig. 12 at $T \leqslant 873$ K are displayed; note that calcination temperatures above 873 K led to a rearrangement of the surface of phosphated Ce oxides [3], making the results at those temperatures no longer comparable. As Fig. 13 clearly shows, at $T_{OSC} = 773$ K the number of equivalent monolayers of O was close to unity for the Ce sample and (as in Fig. 11) decreased continuously for the other phosphated samples. In particular, the number of oxygen monolayers exchanged was 1.1 in the Ce sample, compared with 0.4 in the CeP0.1 and CeP0.2 samples. At higher temperatures ($T_{OSC} = 873$ K), several monolayers of atomic oxygen species were exchanged with $^{18}O_2$(g), indicating that diffusion of O from the inner bulk of the solid to the surface was also deteriorated by P incorporation. In particular, at 873 K only 2.3 and 2.5 monolayers of ^{16}O ($^{16}O_2 + {}^{16}O^{18}O$) were exchanged for the CeP0.1 and CeP0.2 solids, respectively. These values must be compared with the 9.2 monolayers estimated at 873 K for pure CeO_2 to obtain a clearer picture of this phenomenon. This effect is much more intense if we consider the absolute value of μmol of exchanged ^{16}O, not the value shown in Fig. 12, which is normalized to surface area. Therefore, the TPIE results indicate a significant suppression of exchangeable oxygen (both surface and bulk) with increasing P/Ce ratio compared with CeO_2. Once $CePO_4$ was formed, the number of oxygen monolayers exchanged was similar regardless of the amount of P incorporated in the samples. This finding is in harmony with the OSC measurements.

4. Discussion

With respect to the effect of P/Ce ratio on the variation of the OSR properties of phosphated ceria solids, two different regions have been identified. In the samples with low P/Ce ratios (<0.03), incorporation of P results in increased deterioration of OSR properties. In the samples included in this P/Ce ratio domain (CeP0.01 and CeP0.02), only isolated orthophosphate species interacting with Ce(IV) cations predominate. In contrast, in samples with high P/Ce ratios, $CePO_4$ crystals are formed. Once these crystals are formed, further addition of P does not result in a proportional decay of the OSR properties. These results indicate that $CePO_4$ is not the only P species needed for the deterioration of the OSR properties of ceria. Orthophosphate (PO_4) isolated species on the surface and within the subsurface regions of ceria seems also to affect the OSR properties of CeO_2.

The mechanism through which $CePO_4$ can worsen the OSR properties of ceria has been proposed elsewhere [2,5,13,14]. Basically, formation of a crust of $CePO_4$ covering the surface of Ce oxides acts as a main barrier for the OSR between the gas phase and the surface/subsurface of Ce oxides. When $CePO_4$ is formed, part of the Ce surface is blocked against Ce(IV)/Ce(III) redox processes. The presence of a rapid Ce(IV)/Ce(III) redox couple in Ce oxides is a prerequisite for good OSR properties and correct functioning of TWC. Consequently, the presence of a very stable Ce(III) in $CePO_4$ must result in deterioration of the OSR properties.

The presence of orthophosphate species on the surface and within the subsurface regions of ceria also affects the OSR properties of CeO_2. In principle, two mechanisms for the deterioration of OSR properties by PO_4 species can be expected. In the first of these mechanisms, the orthophosphate (PO_4) species anchored at the surface [to Ce(IV) cations] interfere in one of the steps required for surface activation of O species. The formation of coordinatively unsaturated Ce(IV) sites (CUS) on the surface is needed for the activation of oxygen [51], and it can be suppressed because of the poisoning effect of the anchoring of PO_4 species on Ce sites. According to the second mechanism, P(V) cations can inhibit diffusion of oxygen anionic species within the subsurface region.

If suppression of Ce(IV) CUS were involved in the deterioration of the OSR properties of ceria, then variation in these properties by varying the P loading would be expected, similar to the trends described in Figs. 9 and 10. Despite the fact that discontinuity in the surface concentration of Ce was observed in the infrared absorbance of pyridine (Fig. 9) and S_{BET} (Fig. 10), a smooth decline in the OSR properties with increasing P in the low-P/Ce content samples was observed (Figs. 11 and 13). This fact favours the second hypothesis, that inhibition of oxygen anions diffusion within the subsurface region and toward the surface is the predominant mechanism for the deterioration of OSR properties in ceria for the low-P/Ce content samples. In fact, the XPS and NMR results demonstrate that P in the subsurface region increases continuously until $CePO_4$ crystals develop.

The inhibition of oxygen diffusion within the subsurface region of phosphated ceria solids could result from either a reduced number of oxygen vacancies or decreased oxygen mobility. It seems reasonable that oxygen vacancies cannot be formed in Ce–O–P bonds, and thus the number of oxygen vacancies within the subsurface region may decrease. Moreover, it can be suggested that incorporation of P into the CeO_2 lattice may occur through substitution of a Ce(IV) cation with a P (V) cation [54]. Then the charge compensation of the difference in the valence state of Ce and P is expected to be achieved by

the formation of excess oxygen in the framework. This in turn should result in a reduced number of oxygen vacancies.

When surface reorganization occurs in samples with high P/Ce ratio, resulting in the nucleation and formation of large $CePO_4$ crystals, PO_4 units are depleted from the surface and subsurface regions and are found in the monazite crystals. Then the OSR deterioration is restricted to the regions where $CePO_4$ is located, leaving the rest of the surface uncovered by the monazite and free of such deterioration effect. This explains why the formation of $CePO_4$ does not result in an additional decrease in the OSR properties of phosphated ceria solids. The addition of phosphorus seems to cause only enlargement of $CePO_4$ crystals, but a fraction of the surface remains free of P.

5. Conclusions

When P is incorporated into CeO_2, two different domains exist depending on the P/Ce ratio. The borderline should be defined by the P concentration required to saturate the surface by PO_4 units. It is estimated that surface saturation occurs with 5.5 P atoms/nm^2; for the present CeO_2 solid, this is equivalent to a P/Ce ratio of 0.02. The experimental P/Ce ratio is slightly lower than 0.03, however, simply because P also incorporates into the subsurface region of ceria.

For P/Ce values <0.03, only isolated orthophosphate units are detected on the surface and within the subsurface layers of the phosphated Ce oxide. In contrast, at higher P/Ce ratios, only $CePO_4$ crystals are detected. The "border" sample with a P/Ce ratio of 0.03 exhibits isolated PO_4 units and monazite crystals.

PO_4 species on the surface and within the subsurface regions of ceria solid are responsible for the deterioration of the OSR properties of ceria at a low P/Ce ratio, very likely because of the inhibition of oxygen diffusion within the subsurface region of CeO_2. The formation of $CePO_4$ in the phosphated Ce oxide is solely responsible for the deterioration of OSR properties of phosphated ceria at higher P/Ce ratios. The monazite is a very stable Ce(III) phase unable to participate in the Ce(IV)/Ce(III) redox couple required for the optimum functioning of OSR properties of ceria. Once monazite is formed, additional P incorporation does not result in proportional deterioration of OSR properties. Larger monazite crystals are then formed, leaving a fraction of the CeO_2 surface still available for oxygen exchange with gas-phase oxygen.

Acknowledgments

Financial support from the Comunidad de Madrid (GR/AMB/0683/2004) and the Research Promotion Foundation of Cyprus (TEXNO/0603/09) is gratefully acknowledged. F.C.G. thanks the Ministerio de Educación, Cultura y Deportes for an FPU fellowship.

References

[1] C. Larese, F.C. Galisteo, M. López Granados, R. Mariscal, J.L.G. Fierro, M. Furió, R. Fernández-Ruíz, Appl. Catal. B: Environ. 40 (2003) 305.
[2] D. Uy, A.E. O'Neill, L. Xu, W.H. Weber, R.W. McCabe, Appl. Catal. B: Environ. 41 (2003) 269.
[3] C. Larese, F.C. Galisteo, M. López Granados, R. Mariscal, J.L.G. Fierro, Appl. Catal. B: Environ. 48 (2004) 113.
[4] M.J. Rokosz, A.E. Chen, C.K. Lowe-Ma, A.V. Kucherov, D. Benson, M.C.P. Peck, R.W. McCabe, Appl. Catal. B: Environ. 33 (2001) 205.
[5] L. Xu, G. Guo, D. Uy, A.E. O'Neill, W.H. Weber, M.J. Rokosz, R.W. McCabe, Appl. Catal. B: Environ. 50 (2004) 113.
[6] D.R. Liu, J.S. Park, Appl. Catal. B: Environ. 2 (1993) 49.
[7] W.B. Williamson, J. Perry, H.S. Gandhi, J.L. Bomback, Appl. Catal. 15 (1985) 277.
[8] T.N. Angelidis, S.A. Sklavounos, Appl. Catal. A: Gen. 133 (1995) 121.
[9] J. Kašpar, P. Fornasiero, N. Hickey, Catal. Today 77 (2003) 419.
[10] H.S. Gandhi, G.W. Graham, R.W. McCabe, J. Catal. 216 (2003) 433.
[11] M. Shelef, R.W. McCabe, Catal. Today 62 (2000) 35.
[12] R. Di Monte, J. Kašpar, Top. Catal. 28 (2004) 47.
[13] C. Larese, F.C. Galisteo, M. López Granados, R. Mariscal, J.L.G. Fierro, P.S. Lambrou, A.M. Efstathiou, J. Catal. 226 (2004) 443.
[14] C. Larese, M. López Granados, R. Mariscal, J.L.G. Fierro, P.S. Lambrou, A.M. Efstathiou, Appl. Catal. B: Environ. 59 (2005) 13.
[15] P. Duran, M. González, C. Moure, J.R. Jurado, C. Pascual, J. Mater. Sci. 25 (1990) 5001.
[16] R. Fernández-Ruiz, M. Furió, F.C. Galisteo, C. Larese, M. López Granados, R. Mariscal, J.L.G. Fierro, Anal. Chem. 74 (2002) 5463.
[17] C.D. Wagner, L.E. Davis, M.V. Zeller, J.A. Taylor, R.H. Raymond, L.H. Gale, Surf. Interface Anal. 3 (5) (1981) 211.
[18] D. Massiot, Bruker–Franzen Analytik GmbH, Bremen, Germany (1993).
[19] P.S. Lambrou, C.N. Costa, S.Y. Christou, A.M. Efstathiou, Appl. Catal. B: Environ. 54 (2004) 237.
[20] C.N. Costa, T. Anastasiadou, A.M. Efstathiou, J. Catal. 194 (2000) 250.
[21] J. Kašpar, R. Di Monte, P. Fornasiero, M. Graziani, H. Bradshaw, C. Norman, Top. Catal. 16 (2001) 83.
[22] D.R. Mullins, S.H. Overbury, D.R. Huntley, Surf. Sci. 409 (1998) 307.
[23] M. Romeo, K. Bak, J. El Fallah, F. Le Normand, L. Hilaire, Surf. Interface Anal. 20 (1993) 508.
[24] K. Bak, L. Hilaire, Appl. Surf. Sci. 70–71 (1993) 191.
[25] M. Paulis, H. Peyrard, M. Montes, J. Catal. 199 (2001) 30.
[26] M. Daturi, C. Binet, J.C. Lavalley, A. Galtayries, R. Sporken, Phys. Chem. Chem. Phys. 1 (1999) 5717.
[27] P. Burroughs, A. Hamnett, A.F. Orchard, G. Thornton, J. Chem. Soc., Dalton Trans. 17 (1976) 1686.
[28] F.B. Noronha, E.C. Fendley, R.R. Soares, W.E. Alvarez, D.E. Resasco, Chem. Eng. J. 82 (2001) 21.
[29] A.E. Hughes, J.D. Gorman, P.J.K. Patterson, R. Carter, Surf. Interface Anal. 24 (1996) 634.
[30] A. Galtayries, R. Sporken, J. Riga, G. Blanchard, R. Caudano, J. Electron Spectrosc. Relat. Phenom. 88–91 (1998) 951.
[31] T. Masui, H. Hirai, N. Imanaka, G. Adachi, Phys. Status Solidi A 198 (2003) 364.
[32] A.M. Seydoux-Guillaume, R. Wirth, L. Nasdala, M. Gottschalk, J.M. Montel, W. Heinrich, Phys. Chem. Miner. 29 (2002) 240.
[33] H. Onoda, H. Nariai, A. Moriwaki, H. Maki, I. Motooka, J. Mater. Chem. 12 (2002) 1754.
[34] I.L. Mudrakovskii, V.P. Shmachkova, N.S. Kotsarenko, V.M. Mastikhin, Phys. Chem. Solids 47 (1986) 335.
[35] G.L. Turner, K.A. Smith, R.J. Kirkpatrick, E. Oldfield, J. Magn. Reson. 70 (1986) 408.
[36] A.-R. Grimmer, U. Haubenreisser, Chem. Phys. Lett. 99 (1983) 487.
[37] M. Tsuhako, S. Ikeuchi, T. Matsuo, I. Mutooka, M. Kobayashi, Bull. Chem. Soc. Jpn. 52 (1979) 1034.
[38] M. Tsuhako, S. Ikeuchi, T. Matsuo, I. Motooka, M. Kobayashi, Chem. Lett. (1977) 195.
[39] D.W. Breck, Zeolite Molecular Sieves: Structure, Chemistry and Use, Wiley, New Yok, 1974.
[40] Y.X. Ni, J.M. Hughes, A.N. Mariano, Am. Mineral. 80 (1995) 21.
[41] J.M. Lewis, R.A. Kydd, J. Catal. 132 (1991) 465.
[42] M.H. Cao, C.W. Hu, Q.Y. Wu, C.X. Guo, Y.J. Qi, E.B. Wang, Nanotechnology 16 (2005) 282.
[43] H. Onoda, H. Nariai, H. Maki, I. Motooka, Mater. Chem. Phys. 73 (2002) 19.

[44] H. Hirai, T. Masui, N. Imanaka, G. Adachi, J. Alloys Compd. 374 (2004) 84.
[45] T. Masui, H. Hirai, N. Imanaka, G. Adachi, Phys. Status Solidi 198 (2003) 364.
[46] C. Morterra, G. Magnacca, P.P. De Maestri, J. Catal. 152 (1995) 384.
[47] R. Korner, M. Ricken, J. Nolting, I. Riess, J. Solid State Chem. 78 (1989) 136.
[48] J.A. Lercher, C. Grundling, G. Eder-Mirth, Catal. Today 27 (1996) 353.
[49] A. Trovarelli, Catalysis by Ceria and Related Materials, Imperial College Press, London, 2002.
[50] M.I. Zaki, G.A.M. Hussein, S.A.A. Mansour, H.A. El Ammawy, J. Mol. Catal. 51 (1989) 209.
[51] Y. Madier, C. Descorme, A.M. Le Govic, D. Duprez, J. Phys. Chem. B 103 (1999) 10999.
[52] D.J. Cherniak, X.Y. Zhang, M. Nakamura, E.B. Watson, Earth Planet. Sci. Lett. 226 (2004) 161.
[53] M. Boaro, C. de Leitenburg, G. Dolcetti, A. Trovarelli, J. Catal. 193 (2000) 338.
[54] M. Boaro, A. Trovarelli, J.H. Hwang, T.O. Mason, Solid State Ionics 147 (2002) 85.